

Design of Inserts for Split-Hopkinson Pressure Bar Testing of Low Strain-to-Failure Materials

G. Sunny · F. Yuan · V. Prakash · J. Lewandowski

Received: 27 October 2007 / Accepted: 31 March 2008
© Society for Experimental Mechanics 2008

Abstract In the present study a new insert design is presented and validated to enable reliable dynamic mechanical characterization of low strain-to-failure materials using the Split-Hopkinson Pressure Bar (SHPB) apparatus. Finite element-based simulations are conducted to better understand the effects of stress concentrations on the dynamic behavior of LM-1, a Zr-based bulk metallic glass (BMG), using the conventional SHPB setup with cylindrical inserts, and two modified setups—one utilizing conical inserts and the other utilizing a “dogbone” shaped specimen. Based on the results of these computational experiments the ends of the dogbone specimen are replaced with high-strength maraging steel inserts. This new insert-specimen configuration is expected to prevent specimen failure outside the specimen gage section. Simulations are then performed to validate the new insert design. Moreover, high strain-rate uniaxial compression tests are conducted on LM-1 using the modified SHPB with the new inserts. An ultra-high-speed camera is employed to investigate the changes in failure behavior of the specimens. Additional experiments are conducted with strain gages directly attached to the gage section of the specimens to determine accurately their dynamic stress–strain behavior.

Keywords Low strain to failure materials · Split-Hopkinson Pressure Bar · Inserts · Bulk metallic glass · Dogbone specimens

Introduction

The Split-Hopkinson Pressure Bar (schematic shown in Fig. 1) [1–3] is a common technique used in the study of mechanical behavior of materials under high strain-rates (10^2 – 10^4 /s) and uniaxial stress conditions. The technique has been particularly useful in investigating the dynamic behavior of a wide variety of ductile engineering materials (e.g., steels, aluminum alloys, and polymers) [2, 4] after the initiation of plastic flow.

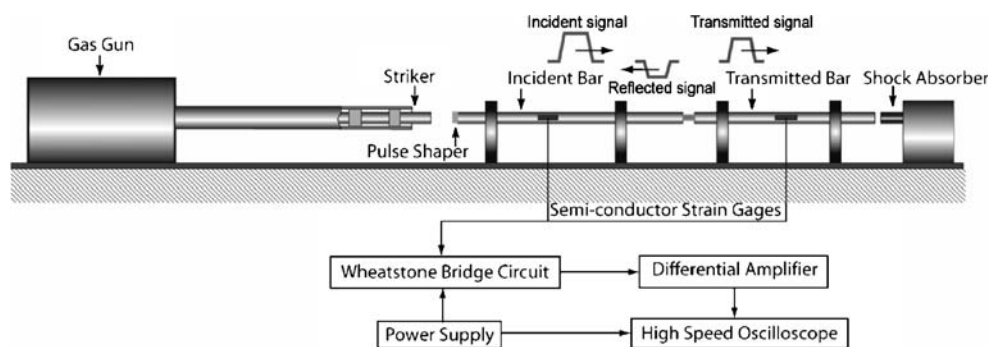
However, the use of the SHPB has been limited on the testing of low strain-to-failure materials such as ceramics, metallic glasses, and rocks, as almost all of the strain exhibited in these materials corresponds to the elastic stress–strain regime. Of particular concern has been the failure of the specimens prior to the attainment of equilibrium conditions within the specimen. These concerns have received considerable attention in the past [5, 6], and have led to the use of stress pulse shapers to prevent premature failure, the use of alternate specimen and insert designs, the use of momentum traps, and an increase in the care of flaw-sensitive specimens. Quasi-static compression testing of brittle and semi-brittle materials pose similar issues regarding constraints, alignment, and effects of lubrication and length-to-diameter (L/D) ratio [7–9].

The design of inserts and specimens has been of significant interest to the research community [5, 6, 10] because of two factors: (a) the inserts can be used to prevent damage to the loading ends of the incident and the

G. Sunny · F. Yuan · V. Prakash (✉, SEM member)
Department of Mechanical and Aerospace Engineering, Case
Western Reserve University,
Cleveland, OH 44106, USA
e-mail: vikas.prakash@case.edu

J. Lewandowski
Department of Materials Science and Engineering, Case Western
Reserve University,
Cleveland, OH 44106, USA

Fig. 1 Schematic diagram of the Split-Hopkinson Pressure Bar (SHPB)



transmitter bars because of the high hardness of certain low strain-to-failure specimens, and (b) the design of the inserts can potentially be used to alleviate the problem of stress concentrations and premature failure in such materials at the specimen/bar interface. Previous investigations involving SHPB along with high-speed photography and optical microscopy have revealed [10] that low strain-to-failure materials can exhibit geometric effects because of stress concentrations arising due to diameter mismatch between the inserts and the specimen [5, 10] in the conventional SHPB experimental setup. In particular, several authors [10–15] have reported both zero and negative strain-rate sensitivities of Zr-based bulk metallic glasses (BMGs) largely because of such geometrical effects.

In particular, the issue of stress concentrations in the testing of low strain-to-failure materials has driven the development of new insert and specimen designs for dynamic testing that will also benefit quasi-static testing. Two alternative designs have been previously suggested [4]—conical inserts in conjunction with a cylindrical specimen, and a dogbone-shaped specimen. The stress distribution in specimens in situations where conical inserts were utilized has been studied in detail [5], and large stress concentrations have been suggested from the simulations. The dogbone specimen, however, has been better characterized because of its potential to promote failure of the specimen within the gage section. The first experiments conducted with the dogbone specimen were performed on AD-94 [16] under quasi-static conditions. Later, SHPB experiments were also performed with dogbone specimens on boron carbide cermets [17, 18], and other tapered samples utilizing chamfered rings to ensure gage section failure in thermoplastics [19]. Additional numerical simulations have been performed on the dogbone specimens to compare their effectiveness to conventional cylindrical specimens [20], as well as other insert-specimen designs [5]. A third alternative design comprised three specimen sections in between two tungsten carbide platens to produce a load train [21].

In the present study a new insert design is presented to enable reliable dynamic mechanical characterization of low strain-to-failure materials using the Split-Hopkinson Pres-

sure Bar (SHPB) apparatus. Finite element-based simulations are conducted to better understand the effects of stress concentrations in specimens using the conventional SHPB setup with cylindrical inserts, and two modified setups—one utilizing conical inserts and the other utilizing a “dogbone” shaped specimen. Based on these results new inserts are developed and subsequently tested using previously well-characterized Zr-based bulk metallic glass ($\text{Zr}_{41.25}\text{Ti}_{13.75}\text{Cu}_{12.5}\text{Ni}_{10}\text{Be}_{22.5}$, LM-1) specimens [22–27]. The simulations indicate a state of stress–equilibrium is achieved within the specimens with the new inserts prior to specimen failure. In order to accurately determine the stress–strain behavior strain gages are additionally applied directly on the specimen surface. These Zr-based bulk metallic glass specimens are observed to exhibit virtually no global plastic strain-to-failure at room temperature and high strain-rates, fail in shear at fracture angles deviant from 45° , and nucleate at the specimen-insert interface during conventional testing [10, 24, 27].

Fig. 2 Schematic of finite element simulation setup to examine stress concentration effects

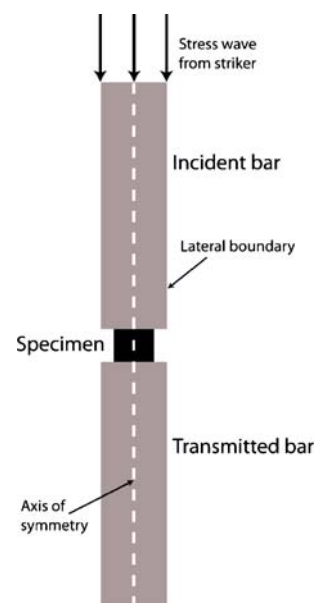




Fig. 3 Additional specimen geometries considered in testing low-ductility materials. (a) Conical inserts, (b) dogbone compression specimen

Stress Concentration at the Specimen/Bar Interface—Finite Element Simulations

To determine the effects of stress concentrations on the dynamic material response, finite element simulations were performed using LS-DYNA-2D to determine the stress distribution in the specimen during the dynamic loading process with different inserts. The schematic of the bar-specimen configuration used for the finite element simulations is shown in Fig. 2. The diameter of the incident and transmitter bars was 19.05 mm, while the diameter of the cylindrical tabs (specimens) was 3.2 mm. Three different specimen sizes with L/D ratios of 6.4, 3.2, and 1.6 mm were used. Both the incident and transmitter bars as well as the specimen were modeled using axi-symmetric rectangular elements. The lengths of the transmitter and incident bars were chosen such that failure in the specimen occurs during the incident compressive pulse. The dimension of the finite elements along the radial direction was 0.05 mm for all elements; along the axial direction the element size in the bars varied from 0.05 mm (near the insert-specimen interface) to 1.7 mm (at the ends of the incident and transmitted bars); the size of all the finite elements within the specimen was 0.05 mm.

In addition, finite element simulations were performed with conical inserts (radius 9.525 mm at the insert-bar interface and radius 1.6 mm at the insert-specimen interface) and “dogbone” specimens (radius 9.525 mm at the insert-bar interface and radius 1.6 mm in the center). For these simulations, rectangular elements were used in the gage section of the specimen and in the incident and transmitted bars, while primarily quadrilateral and some

triangular elements were used in the conical inserts and outside the gage section of the dogbone specimen. The element size varied from 0.05 mm (in the specimen and near the specimen-insert interface) to 1.7 mm (at the ends of the incident and transmitted bars). Schematic figures for the conical inserts and the dogbone specimen are shown in Fig. 3.

For all simulations an initial condition consistent with prescribed particle velocity (i.e. the impact velocity) and zero stress was used. These conditions were maintained for a long enough time so that no release waves from the bar ends arrived at the specimen prior to specimen failure. The LM-1 specimen was modeled as a bilinear elastic-plastic material, consistent with previous experimental observations [11, 13, 15, 24, 27]. The mechanical properties of the materials (i.e., Young’s Modulus, yield strength, failure strength) are shown in Table 1.

The axial stress distribution in the specimen using the conventional SHPB experimental setup (i.e. cylindrical inserts and specimen) is shown in Fig. 4(a). It is apparent that a significant stress concentration develops in the specimen regardless of the specimen L/D ratio. However, the magnitude of the stress concentration varies with the L/D ratio—for a L/D ratio of 2.0 the stress concentration is ~ 1.4 while for $L/D=0.5$ the stress concentration increases to ~ 1.7 . The shear stress distribution in the specimen for the case of the conventional SHPB setup is shown in Fig. 4(b). Like in the case of the axial stress, a shear stress concentration develops in the specimen which leads to elevated shear stresses. These shear stresses, however, appear to be fairly small in magnitude and would likely play a role only in combination with large axial stresses. It is also apparent that the maximum shear planes are oriented at approximately 50° from the longitudinal axis, and this angle is constant regardless of the L/D ratio. This observation is consistent with previous fracture plane angle measurements in LM-1 [24, 27]. The orientation of the shear plane also suggests a cause for the change in failure mechanisms with a decrease in the L/D ratio; for the case of smaller L/D ratio specimens ($L/D=0.5$) the fracture instability that results after the formation of the first shear failure

Table 1 Selected material properties of the BMG [22, 24, 26, 27], maraging steel, and tungsten carbide used in the simulations

	LM-1 (BMG)	Maraging steel	Tungsten carbide
Young’s Modulus (GPa)	96 (elastic), 9.6 (plastic)	210	675
Density (kg/m^3)	6,000	7,800	15,700
Wave speed (m/s)	4,000	5,190	6,560
Impedance ($\text{kg/m}^2 \text{ s}$)	24×10^6	40.5×10^6	103×10^6
Yield strength (GPa)	2.0	2.5	10
Poisson’s ratio	0.33	0.30	0.20

Maraging steel and tungsten carbide data were supplied by Dynamic Metals International and Cermet, respectively.

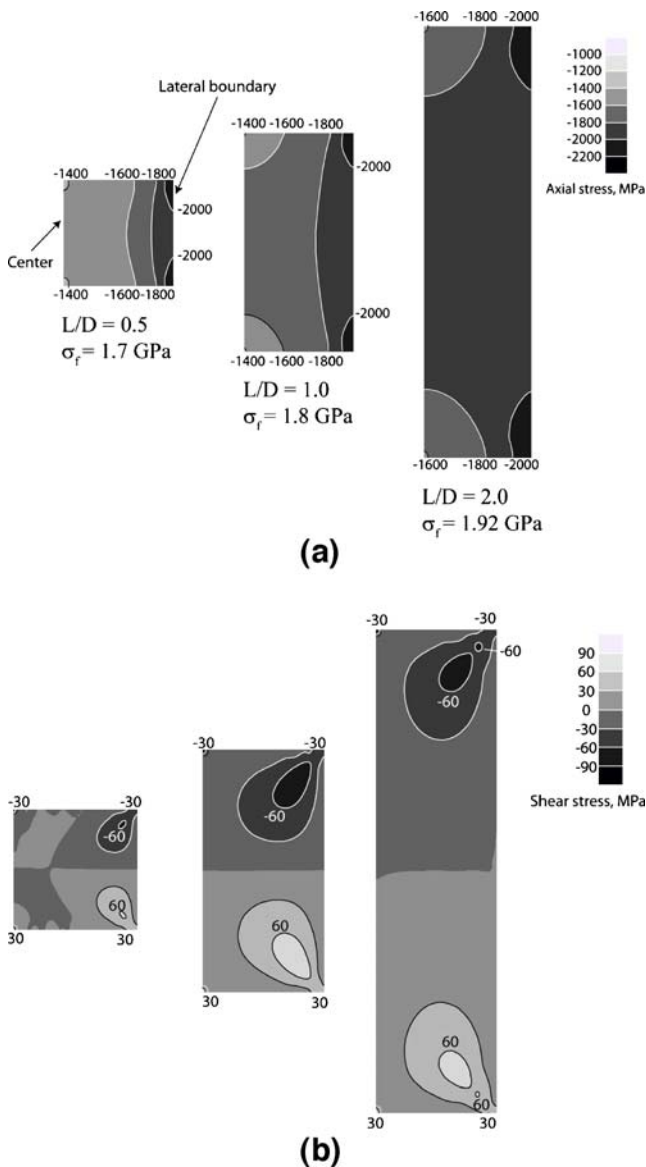


Fig. 4 (a) Axial and (b) shear stress contours for finite element simulations of LM-1 with cylindrical inserts for L/D ratios of (left) 0.5, (middle) 1.0, and (right) 2.0. All stress contours are shown except those of zero stress

is unable to continue unimpeded through the diameter of the specimen due to geometrical and specimen size constraints. Multiple shear failures can occur in the specimen sandwiched between the compression platens before complete failure of the specimen.

The axial and shear stress distributions in the specimen tested with the conical inserts are shown in Fig. 5. As for the cylindrical inserts, an inhomogeneity in the axial stress state is apparent, as shown in Fig. 5(a). From the stress contours a stress concentration of approximately 1.3 can be estimated, with peak stresses occurring at the circumferential boundary at the insert-specimen interface, which is also in agreement with the stress distribution in the conventional

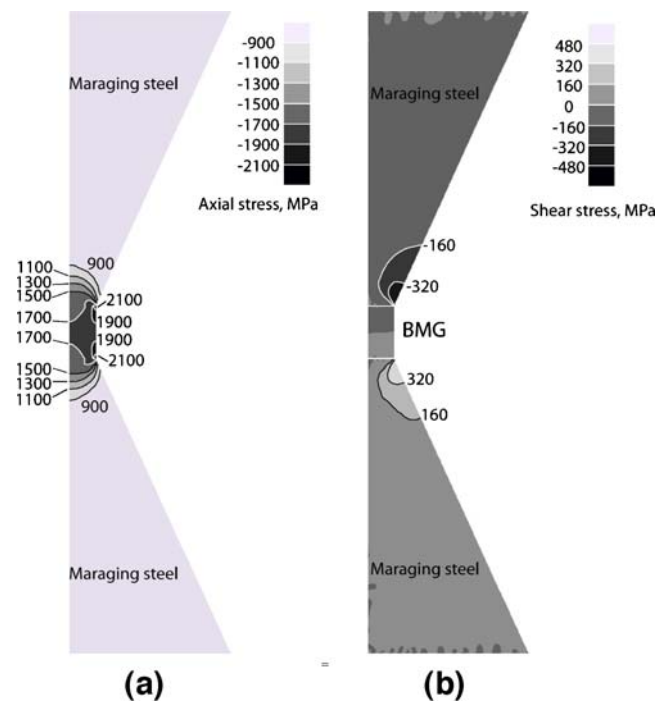


Fig. 5 (a) Axial and (b) shear stress contours for simulation with conical inserts. All stress contours are shown except those of zero stress

SHPB setup. In addition, there are large shear stresses at the insert-specimen interface, as shown in Fig. 5(b), which, with the elevated stresses, can contribute to premature failure of the specimen.

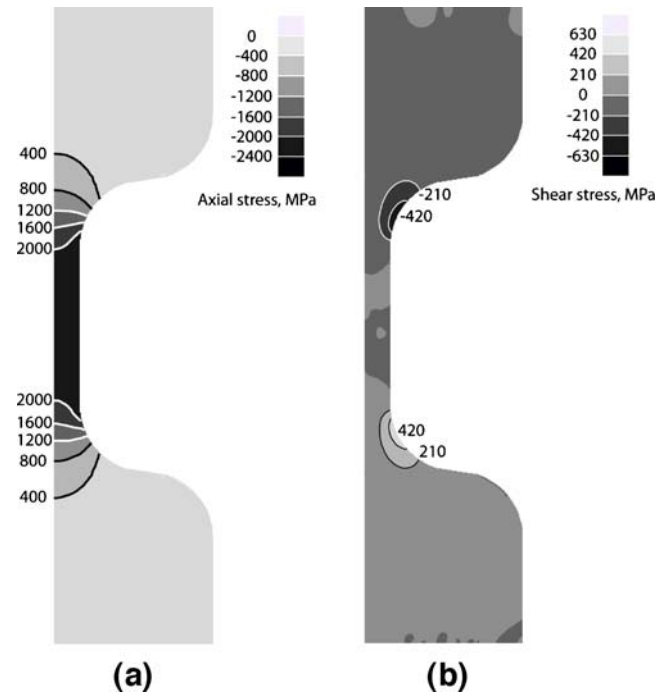
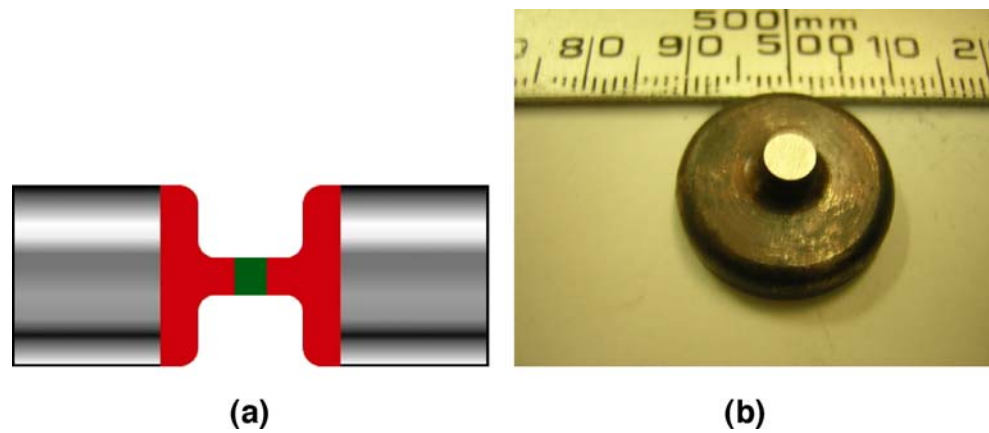


Fig. 6 (a) Axial and (b) shear stress distribution of dogbone specimen. All stress contours are shown except those of zero stress

Fig. 7 (a) Schematic of new insert design, (b) actual design



The axial and shear stress distributions for the dogbone specimen are shown in Fig. 6(a) and (b), respectively. Based on the axial stress contours there does not appear to be a stress concentration in the gage area of the specimen, and the gage area exhibits a nominally uniform stress state. However, the shear stress contours indicate large shear stresses (upwards of 30% of the yield stress) just outside of the gage section of the specimen. These high shear stresses could be particularly problematic because shear, coupled with axial stresses, can lead to failure of relatively low strain-to-failure material specimens outside their gage sections.

Design and Development of the New Inserts

In addition to the stress concentrations present in the specimen, the machinability of the specimens/inserts and the ability to test a wide range of specimens must be considered. Conical inserts are somewhat challenging to machine, especially when conical ceramic (e.g., WC) inserts are desired, but they are not typically difficult to machine from maraging steel. Dogbone specimens, on the other hand, can be prohibitively expensive to machine because of the complicated geometry. In addition, most bulk metallic glasses are unsuitable for the dogbone geometry, as the maximum thicknesses available (while ensuring fully amorphous specimens) are no more than 10 mm (and often closer to 5 mm).

In the present study, in order to address these issues, the ends of the dogbone specimen are replaced with maraging steel inserts, which is stronger than the LM-1 BMG material. In this way, part of the gage section of the specimen is made out of LM-1, and the remaining part of the experimental setup consists of contoured maraging steel (Vascomax 350) inserts, as shown in Fig. 7. Use of the maraging steel prevents failure due to shear in the transition region where the diameter is reduced because of the relatively high yield strength of the maraging steel (~2.5 GPa). In addition, maraging steel can be easily machined, as it has a much lower hardness ($R_C=33$) when compared to LM-1 ($R_C=60$) prior to annealing, so that the diameters of the reduced insert and the specimen can be matched. Finally, use of the maraging steel inserts no longer requires large-sized specimens, as the reduced insert diameter can be chosen to match the specimen diameter. Specimens with higher yield strengths (i.e. >2.5 GPa) will require the use of higher strength inserts as the maraging steel will likely yield or fail prior to specimen failure.

A finite element simulation was performed with the new dogbone inserts in the same way as the previous simulations. The resulting axial and shear stress contours are shown in Fig. 8. In both cases, a nominally uniform state of

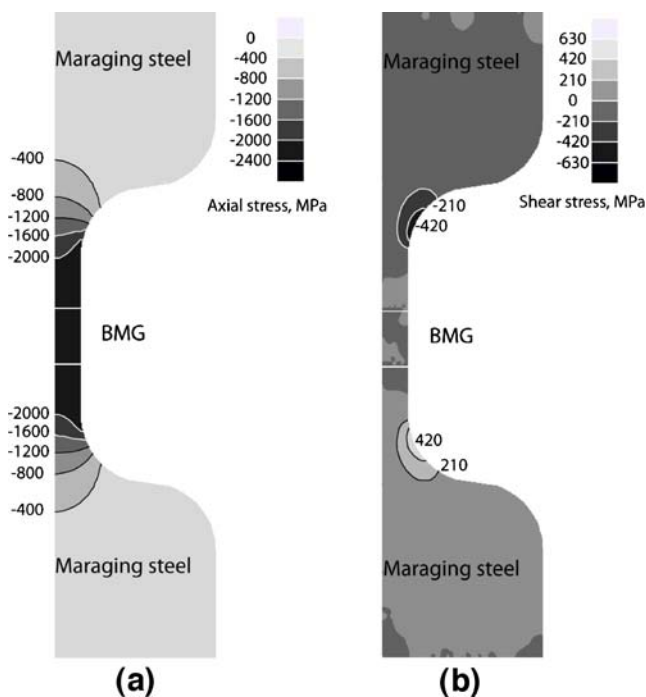


Fig. 8 (a) Axial and (b) shear stress distribution for simulation with maraging steel inserts. All stress contours are shown except those of zero stress

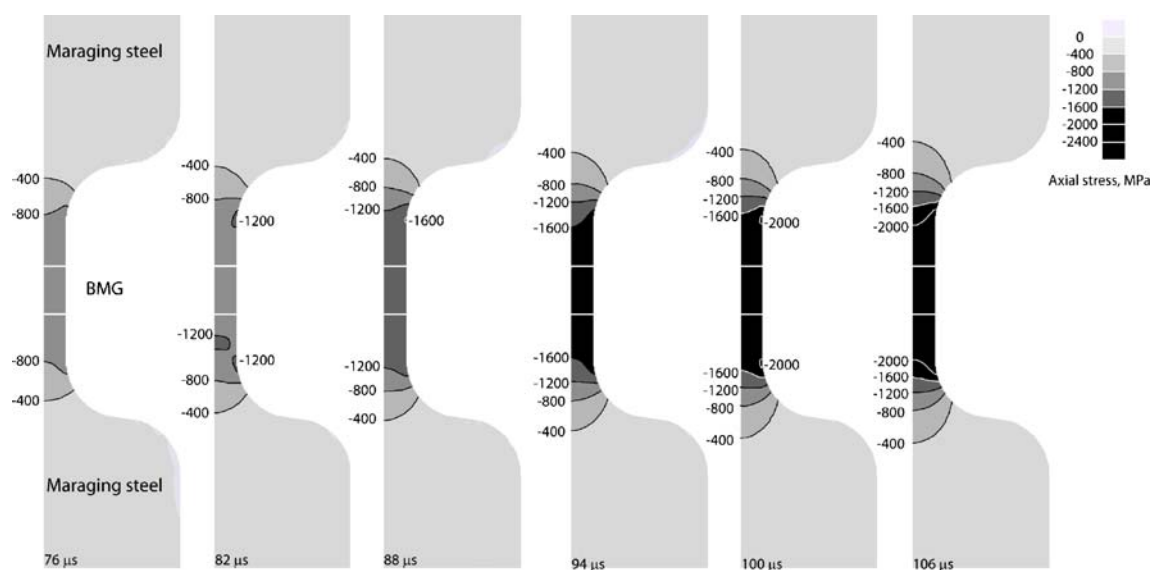


Fig. 9 Evolution of the axial stress state in the dogbone specimen, with times marked

axial stress is attained within the specimen, such that the build-up of stress concentration is minimized. Also, there is very little shear stress in the specimen (less than 120 MPa, or 6% of the peak stress, based on the simulation), so premature failure is not expected at the insert-specimen interface. In addition, since the maximum axial and shear stresses in the insert (2.0 GPa and 500 MPa) are less than the yield strength (~ 2.5 GPa) of the maraging steel insert, failure in the insert is not expected. The time evolution of the stress state within the specimen is shown in Fig. 9; a uniform stress state (corresponding to a stress level of 1.0 GPa) is attained within the specimen, which is well before the failure of the LM-1 BMG specimen.

SHPB Experiments on LM-1 with the New Inserts

A Split-Hopkinson Pressure Bar (SHPB) was employed to conduct the high strain-rate compression tests on specimens of LM-1 using the new inserts. The facility comprises a striker bar, an incident bar and a transmitter bar, all made from 19.05 mm diameter high-strength maraging steel having a nominal yield strength of 2,500 MPa. Striker bars with lengths of 200 mm were used in the present study. The incident and transmitter bars were approximately 1.5 and 1.4 m in length, respectively, and they were previously centerless ground to ensure that the ends are parallel to within 10 μm , in accordance with specifications noted before [4]. The striker bar was accelerated using an air operated gas gun. A pair of semiconductor strain gages (BLH SPB3-18-100-U1) are strategically attached on the incident and transmitter bars and are used in combination with a Wheatstone bridge circuit connected with a differential amplifier (Tektronix 5A22 N) and a digital

oscilloscope (Tektronix TDS 420) to monitor the strain pulses during the test. Vacuum grease was placed at the interfaces between the “dogbone” inserts and the respective bars, while molybdenum disulfide grease was placed at the insert-specimen interfaces. To better understand the failure process of LM-1, a high speed camera, Hadland IMACON 200, with a maximum framing rate capability of 200 million frames per second was used to image the failure process.

The LM-1 BMG specimens were received in the form of plates (90 \times 63 \times 5) mm from Liquidmetal, Inc. and were verified to be amorphous [23–25, 27]. The plates were electrical discharge machined into rectangular bars and then centerless ground to long rods of diameter 4 mm to ensure

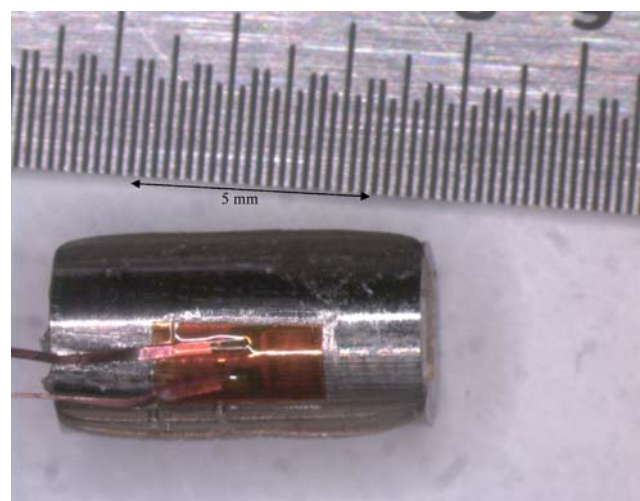


Fig. 10 Specimen with strain gage attached, prior to removal of epoxy and detachment of leads. The barreled appearance of the specimen is due to the presence of epoxy

the faces are parallel to within 10 μm . After metallographic polishing of the rods, they were cut using a Buehler low-speed saw into tabs with $L/D=0.5\text{--}2.0$, and then lapped and polished to a 6 μm finish to ensure that the compression surfaces were flat and parallel.

While the new inserts mitigate the effects of stress concentrations, they do deform elastically during the dynamic loading process, especially in the transition region of reduced cross-sectional area near the specimen/insert interface. This mandates strain gages be applied directly to the specimen to accurately determine the stress–strain response of the specimens during the dynamic loading process. In the present study, strain gages (EA-06-031CE-350 with attached leads, Vishay Micromeritics Group) were placed directly on 4 mm diameter specimens ($L/D=1.0$ and 2.0) of amorphous LM-1, as shown in Fig. 10. The “barreled” appearance of the specimen in the figure is due to the presence of epoxy and not compression testing; the excess epoxy was removed from the specimen faces prior to testing. Besides conducting experiments with strain gages on the specimens, a series of experiments were also conducted without strain gages on the samples in order to examine the changes in the failure mode of the LM-1 due to the new inserts. To that end, an ultra-high speed camera (Imacon 200) was employed to take pictures of the deformation and failure of the LM-1 specimens.

Copper pulse shapers of dimensions (8 \times 8 \times 0.75) mm were utilized in all experiments to increase the rise time of the incident stress so as to reduce the likelihood of premature failure of the LM-1 specimens. The strain history signals for a representative experiment are shown in

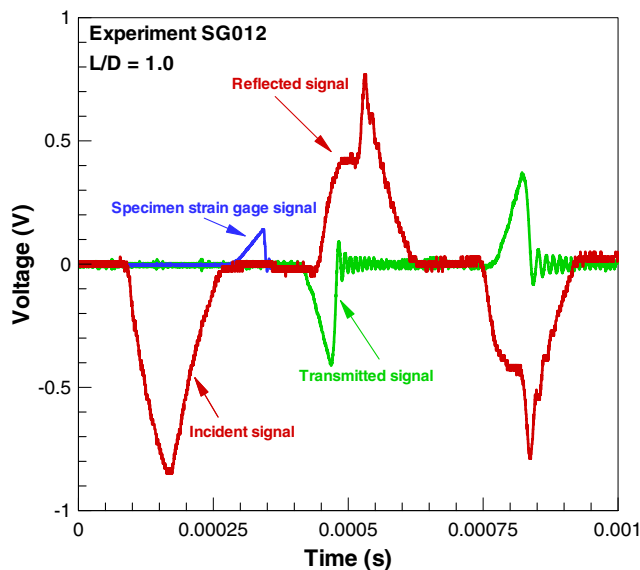


Fig. 11 Strain history signals from the strain gages mounted on the incident bar, transmitted bar, and specimen

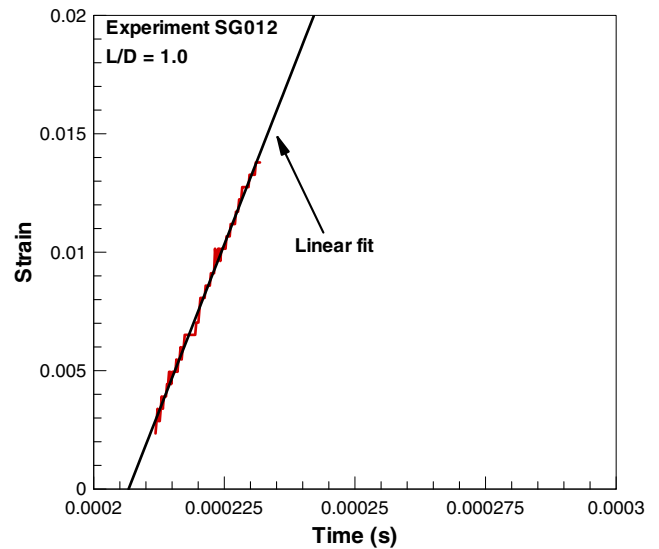


Fig. 12 Selected strain history as determined from the strain gage in Fig. 11. Based on the linear fit, the specimen is deforming under constant strain-rate conditions

Fig. 11. As can be seen in the figure, the incident and transmitted pulses have nominally similar slopes. The strain gage history of the gage on the specimen shows a linear strain vs. time profile, as seen in Fig. 12, which suggests that the specimens deform at a nominally constant strain-rate during the dynamic compression loading process. The stress–strain curve for this experiment is shown in Fig. 13. A linear elastic behavior for the specimen is assumed ($E=96$ GPa, consistent with previous dynamic experiments [28]) in the construction of the stress–strain response from the measured strain gage signal.

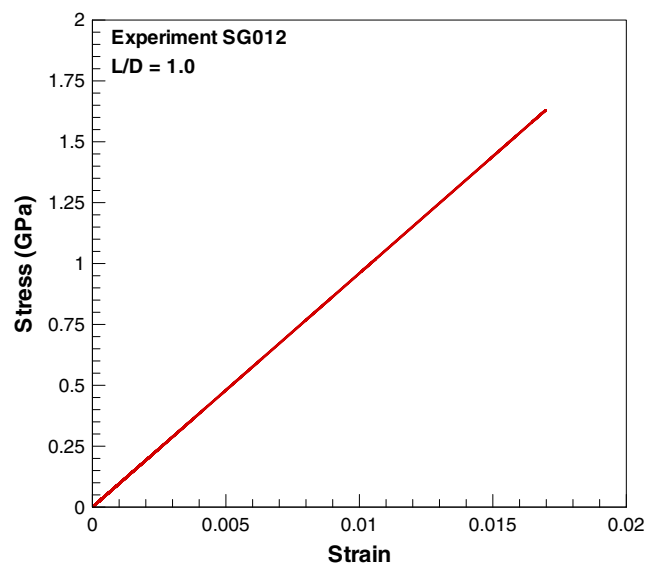
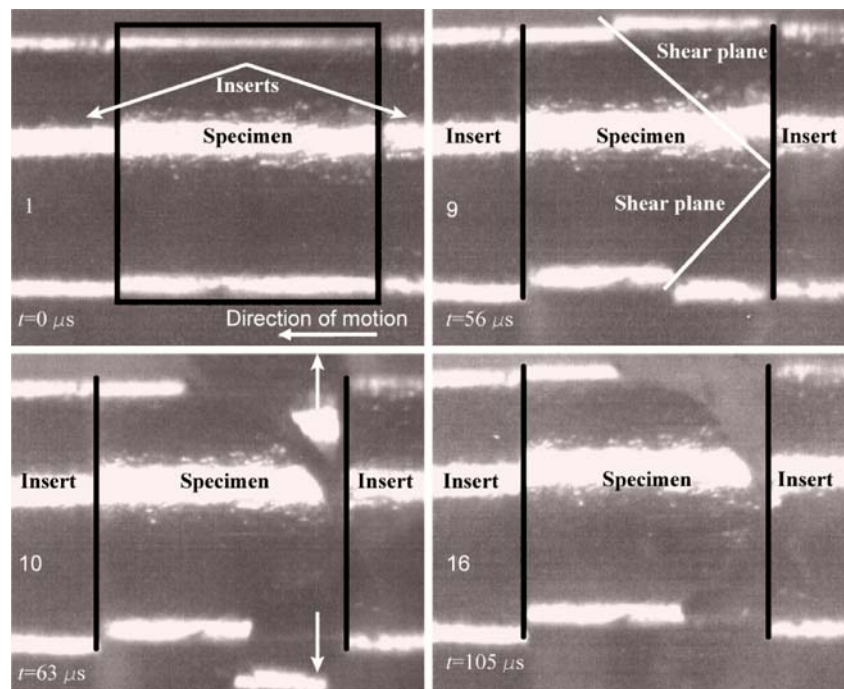


Fig. 13 Stress–strain curve constructed from the specimen strain gage signal in Fig. 11

Fig. 14 High-speed camera images of as-cast LM-1 ($L/D=1.0$) with new tapered inserts

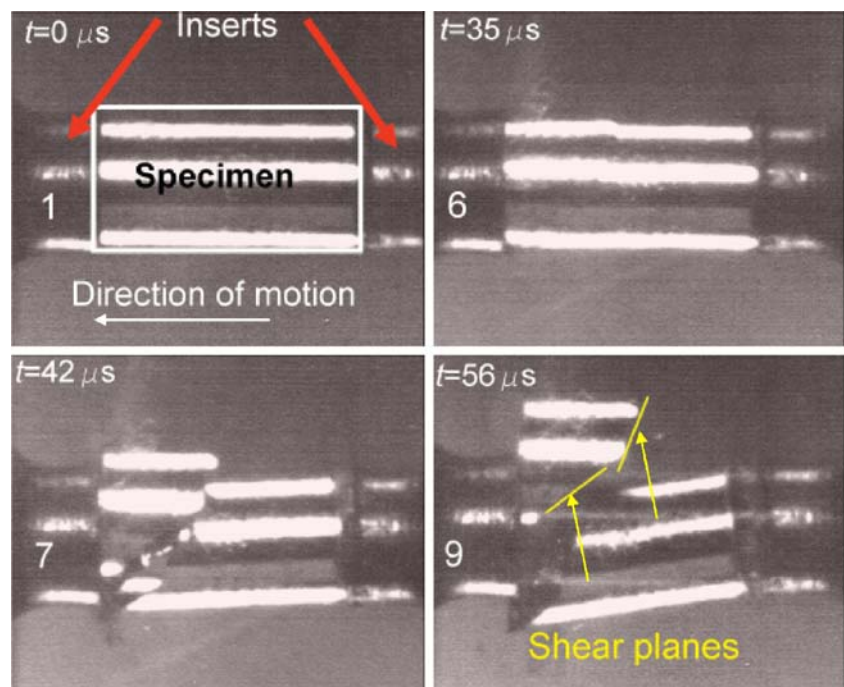


Experimental Results and Discussion

High-speed camera images (with an inter-frame time of $7 \mu s$) of an experiment conducted on as-cast LM-1 with the new inserts are shown in Fig. 14. The specimen ($L/D=1.0$) is initially unstressed (Frame 1), but as the stress wave loads the specimen (Frame 9), two shear planes form in the

gage region of the specimen, leading to catastrophic failure of the specimen (Frame 10). Due to the forward momentum of the remainder of the specimen, it penetrates the insert on the incident bar (Frame 16). Unlike that observed in previous experiments, where failure initiated at the specimen/insert interface [10], in the tapered insert geometry specimen failure occurs in the gage section. Similar results

Fig. 15 High-speed camera images of as-cast LM-1 ($L/D=2.0$) with new tapered inserts



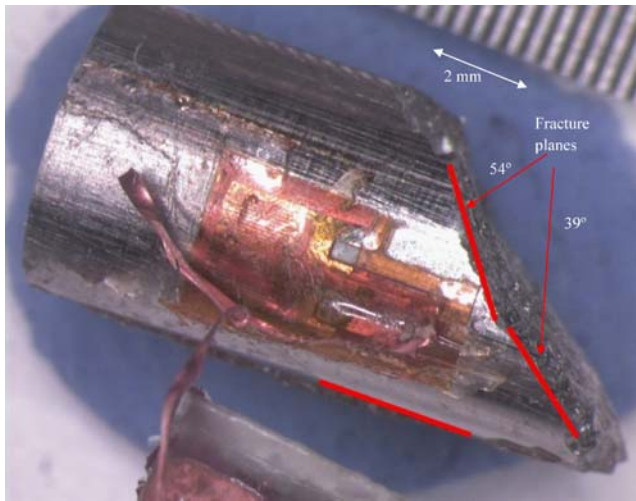


Fig. 16 Optical microscopy of as-cast specimen, $L/D=2.0$, after testing, with strain gage present and fracture angles noted

were obtained with a LM-1 specimen with $L/D=2.0$, as shown in Fig. 15. The intact specimen prior to loading is shown in Frame 1. An instability is clearly evident in the top half of the sample (Frame 6) which is fully contained within the gage section of the specimen. Two shear planes with different orientations are clearly seen in Frame 7, with the final separation in Frame 9. This behavior consistently occurs in specimens with $L/D=2.0$, regardless of whether or not strain gages are applied, as seen in Fig. 16.

The results of the experiments conducted on specimens with $L/D=2.0$ are shown in Table 2. Of the five specimens tested, two of them failed prior to separation of the strain gage from the specimen, one did not fail during the test, and two specimens failed after the strain gage separated from the specimen (implying that the strain gage did not capture the entire strain history of the specimen). For the two specimens which failed before delamination of the strain gage, the strain measured was approximately 1.8% and 1.9%, corresponding to a peak stress range of 1.73–1.82 GPa.

Likewise, the results of the experiments conducted on specimens with $L/D=1.0$ are shown in Table 3. Eight specimens were tested in this group; of the eight specimens, four failed prior to separation of the strain gage from the specimen, three specimens failed after separation of the

strain gage, and one specimen did not fail during testing. For the specimens that failed prior to delamination of the strain gage, the peak strain measured was between 1.7% and 2.2%, corresponding to a peak stress range of 1.63–2.00 GPa.

Comparing the results of the experiments obtained by using the new inserts in the present study with those from an earlier study using the conventional cylindrical inserts [10], reveals several key differences. First, it is apparent that the use of the new tapered inserts changes the deformation and fracture behavior of as-cast LM-1, with failure occurring in the gage section of the specimen. In addition, the fracture planes of the as-cast specimens are different; instead of single shear planes which nucleated at the specimen-insert interface in the experiments conducted with cylindrical inserts, fracture initiates in the gage section and more than one fracture angle is exhibited in these experiments. Second, while there was a slight decrease in the peak stress with decreasing L/D in the tests conducted with the cylindrical inserts [10, 12, 15], the difference in the peak stress levels attained in the tests conducted with the new inserts is less than 10%. Finally, the use of the strain gages also allows a more accurate determination of the elastic stress-strain response of the specimen.

As noted before, the use of the new tapered inserts requires the use of strain gages directly mounted on the specimen. Typical stress versus strain time curves for LM-1 are shown in Fig. 17, while the peak stresses (as determined from strain gage measurements on the bar and the specimen) are shown in Fig. 18 for the six successful experiments (in which specimen failure occurred prior to separation of the strain gage from the specimen). Based on Fig. 18, the differences in the peak stresses as determined from the transmitted bar and the specimen strain gage signals are within 10% of each other. This 10% variation in the peak stresses is a typical experimental error for tests conducted on the Hopkinson Bar for materials exhibiting low strains-to-failure, as noted elsewhere [11, 29].

In contrast, the differences in the strains and strain-rates as inferred from the strain gage signals on the specimen and the reflected bar can be quite large. Figure 19 shows the strain vs. time curve for experiment SG12 as determined from both the reflected bar and the specimen strain gage

Table 2 List of experiments conducted with specimens with $L/D=2.0$

Experiment	Striker velocity (m/s)	Peak strain (%)	Peak stress (MPa)	Specimen failed?	Strain gage separated?
SG001	7.9	1.41	1,350	Yes	Yes (invalid)
SG002	8.0	1.61	1,550	Yes	Yes (invalid)
SG003	7.2	1.55	1,490	No	No
SG004	8.8	1.89	1,810	Yes	No (valid)
SG005	10.3	1.83	1,750	Yes	No (valid)

Table 3 List of experiments conducted on specimens with $L/D=1.0$

Experiment	Striker velocity (m/s)	Peak strain (%)	Peak stress (MPa)	Specimen failed?	Strain gage separated?
SG006	8.2	1.50	1,440	Yes	Yes (invalid)
SG007	7.3	0.92	880	No	No
SG008	10.2	1.97	1,890	Yes	No (valid)
SG009	7.8	1.41	1,340	Yes	Yes (invalid)
SG010	9.4	0.91	870	Yes	Yes (invalid)
SG011	8.5	1.95	1,870	Yes	No (valid)
SG012	9.0	1.70	1,630	Yes	No (valid)
SG013	8.8	2.2	2,000	Yes	No (valid)

In experiment SG13, the specimen was assumed to yield prior to failure

signals. Compared to the strain-rate determined from the specimen strain gage (Fig. 11, 550/s), the strain-rate determined from the the reflected bar (at the time of failure) is 1,200/s, which is more than double the strain-rate obtained from the specimen strain gage. In addition, the strain-rates for all experiments as obtained from the specimen strain gage are much lower than calculated from the reflected signal, as shown in Fig. 20. Thus, even though the transmitted bar signal can be used to obtain the stress in the specimen with the new inserts, the use of the reflected signal for calculating strain and strain-rate is questionable and is expected to lead to errors. The discrepancy in the measured strain-rates can be explained by considering the following equation to calculate the strain-rate of the specimen in a conventional SHPB experiment:

$$\dot{\varepsilon} = -2 \frac{c_b}{l_s} \varepsilon_R(t), \quad (1)$$

where $\dot{\varepsilon}$ is the strain-rate, c_b is the wave speed in the bar, l_s is the specimen length, and $\varepsilon_R(t)$ is the strain in the

reflected bar as a function of time. For the conventional SHPB experiments using maraging steel inserts [10], the insert diameter is approximately five times the specimen diameter, so that the average stress generated in the steel inserts is 4% of the stress in the specimen. Assuming linear elastic behavior of the steel ($E=210$ GPa) and the LM-1 specimen ($E=96$ GPa), this means the strain of each of the steel inserts is approximately 2% of the total strain recorded by the bars. However, in the new insert design (Fig. 7), part of each of the steel inserts (approximately 2 mm, or half the length of the specimen) is the same diameter as the specimen. Assuming that the strain-rate in the specimens used in the present study can be approximated by equation (1), the axial deformation of the inserts accounts for up to half of the total strain recorded by the reflected signal. Therefore, the strain history inferred using the reflected strain gage signal is not valid in the calculation of the strain-rates and strains experienced by the specimen.

In Fig. 21, the peak stresses in the as-cast LM-1 (in the present study) are superimposed on the peak stresses achieved with the cylindrical inserts [10]. In addition, data

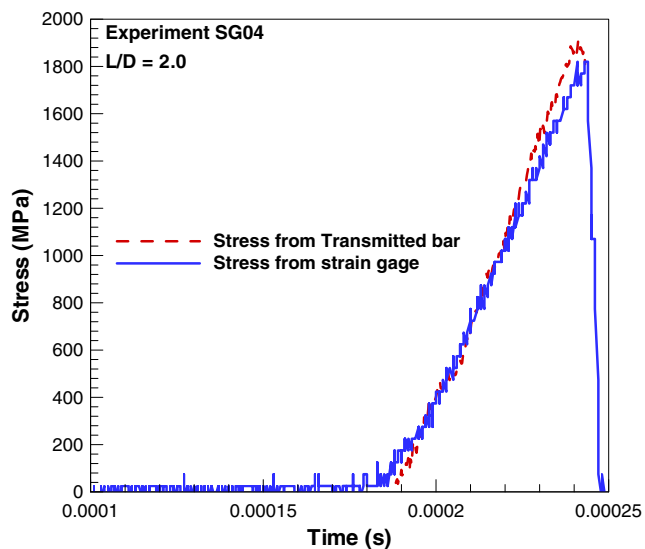


Fig. 17 Comparison of stress signals as determined from the transmitted bar and specimen strain gage

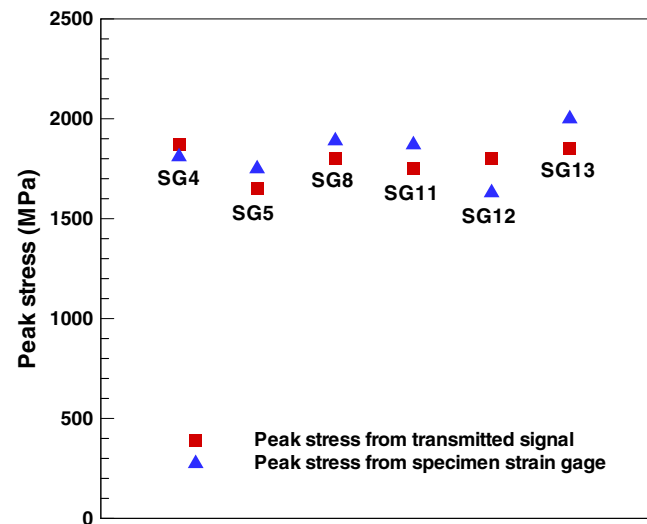


Fig. 18 Peak stresses as determined from transmitted and specimen strain gage signals

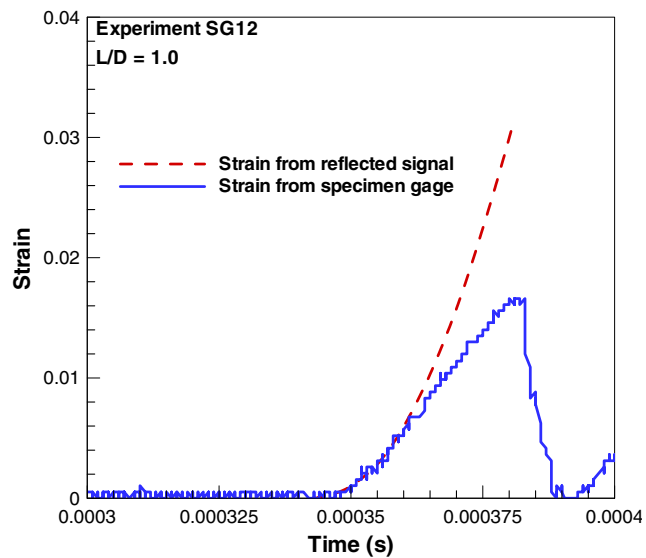


Fig. 19 Strain vs. time plots as determined from the reflected signal and from the specimen strain gage. Thus, the strain-rate calculated (from the slope of the curve) is much higher than the actual strain-rate experienced by the specimen

from Bruck's work on LM-1 [11] are also shown in the figure. Based on these data it is apparent that the reduction in the stress concentration factor due to the inserts somewhat reduces the scatter in the peak stresses for the lower L/D specimen ratios. In addition, in Bruck's experiments [11], it appears that the peak stresses from the specimen strain gages are on the high side of the range (although not statistically different) of the peak stresses from the transmitted bars. While some stress triaxiality is present in the gaged samples in Bruck's experiments (because of the cylindrical inserts and the small aspect

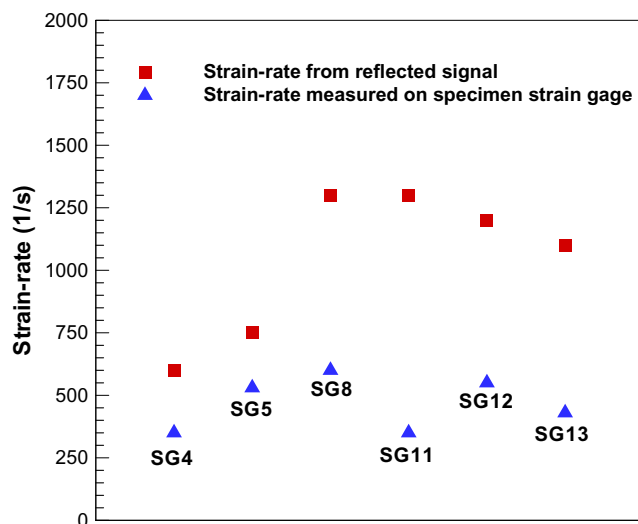


Fig. 20 Peak strain-rates as measured from the reflected signal compared to constant strain-rates as measured from the specimen strain gage

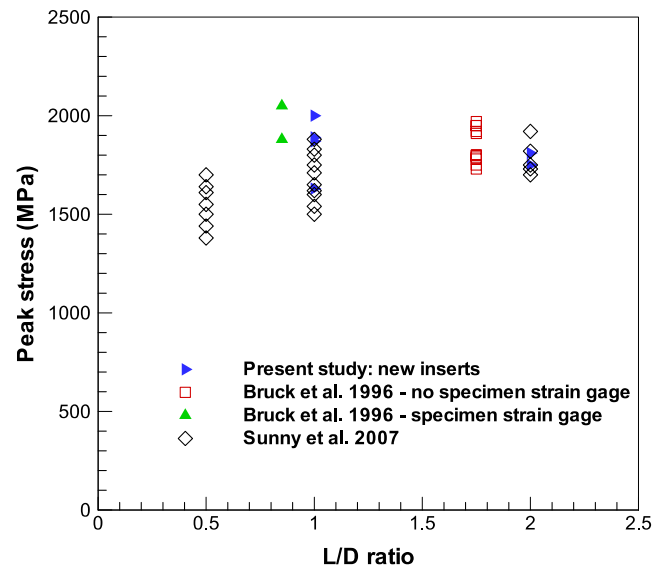


Fig. 21 Peak stress achieved by as-cast LM-1 specimens with new inserts. Data from Sunny et al. [10] and Bruck et al. [11] are also included

ratio) the stress state in the experiments conducted with the new tapered inserts is expected to be nearly uniaxial.

Summary

1. Elevated normal and/or shear stresses due to stress concentrations are present in low strain-to-failure materials due to the diametral mismatch between the inserts and the specimen in SHPB experiments. These are also present when conical inserts or dogbone specimens are utilized.
2. A dogbone insert design has been developed based on finite element simulations of the SHPB and has been shown to mitigate the stress concentrations present.
3. Strain gages and an assumed stress-strain curve are necessary with the new insert design because of the elastic deformation of the inserts especially in the region of reduced cross-sectional area near the specimen-insert interface.
4. The new inserts clearly promote failure in the gage section of LM-1, compared to failure at the specimen-insert interface in conventional SHPB experiments.
5. The use of strain gages and appropriate pulse shaping can provide a constant strain-rate at very low (e.g. 0.3%) strains.
6. For this new experimental setup, the peak stresses as determined from the transmitted bar and the specimen strain gage are within the experimental error. The deformation of the maraging steel inserts accounts for the large difference between the peak strain-rates as measured from the specimen strain gage signal and the reflected signal.

7. The dogbone inserts and strain gages appear to show an increase in the peak strength of the LM-1 tested.

Acknowledgments The authors acknowledge Xin Tang and Ali Shamimi Nouri for discussions and experimental support, and Liquidmetal, Inc. for producing and supplying some of the bulk metallic glass plates used in the experiments. Partial funding for this work is provided by a Case Prime Fellowship (GS, FY), ONE-N00014-03-1-0205, and DARPA-ARO-DAAD19-01-0525. Additional experimental support is provided by the U.S. Department of Energy (DOE), Corrosion and Materials Performance Cooperative, DOE Cooperative Agreement Number: DE-FC-28-04RW12252. This work is in support of the Defense Advanced Research Projects Agency, Defense Science Office, and the DOE Science & Technology Program of the Office of the Chief Scientist, Office of Civilian Radioactive Waste Management program for development of corrosion resistance of iron-based amorphous metal coatings under direction of Dr. J.C. Farmer at Lawrence Livermore National Laboratory. Funding for the high-speed camera was provided by NSF MRI, CMS 0079458.

References

- Davies RM (1948) A critical study of the Hopkinson pressure bar. *Philos Trans R Soc Lond Ser A* 240:375–457.
- Kolsky H (1949) An investigation of the mechanical properties of materials at very high rates of loading. *Proc Phys Soc, B* 62:676–700.
- Hopkinson B (1914) A method of measuring the pressure produced in the detonation of high explosives or by the impact of bullets. *Philos Trans R Soc Lond, A* 213:437–456.
- Gray GT (2000) Classic split-Hopkinson pressure bar testing. *American Society for Materials Handbook*, 8th edn. American Society for Materials International, Materials Park, OH, pp 462–476.
- Chen W, Subhash G, Ravichandran G (1994) Evaluation of ceramic specimen geometries used in split-Hopkinson pressure bar. *Dymat Journal* 1:193–210.
- Subhash G, Ravichandran G (2000) Split-Hopkinson pressure bar testing of ceramics. *American Society for Materials Handbook*, 8th edn. American Society for Metals International, Materials Park, OH, pp 497–504.
- Paterson MS (1978) *Experimental rock deformation—the brittle field*. Springer, New York.
- Peng S, Johnson AM (1972) Crack growth and faulting in cylindrical specimens of Chelmsford granite. *Int J Rock Mech Min Sci* 9:37–86.
- Zeuch DH (1992) Comment on “Plastic deformation and fracture behavior of a Fe-modified Al_3Ti -base $L1_2$ intermetallic alloy”: the importance of specimen length-to-width ratios and end constraints in compression testing of brittle and semi-brittle materials. *J Mater Res* 7:1956–1959.
- Sunny G, Prakash V, Lewandowski JJ (2007) Effects of annealing and specimen geometry on dynamic compression of a Zr-based bulk metallic glass. *J Mater Res* 22:389–401.
- Bruck HA, Rosakis AJ, Johnson WL (1996) The dynamic compressive behavior of beryllium bearing bulk metallic glasses. *J Mater Res* 11:503–511.
- Hufnagel TC, Jiao T, Xing LQ, Ramesh KT (2002) Deformation and failure of $Zr_{57}Ti_5Cu_{20}Ni_8Al_{10}$ bulk metallic glass under quasi-static and dynamic compression. *J Mater Res* 17:1441–1445.
- Lu J, Ravichandran G, Johnson WL (2003) Deformation behavior of the $Zr_{41.2}Ti_{13.8}Cu_{12.5}Ni_{10}Be_{22.5}$ bulk metallic glass over a wide range of strain-rates and temperatures. *Acta Mater* 51:3429–3443.
- Subhash G, Dowding RJ, Kecskes LJ (2002) Characterization of uniaxial compressive response of bulk amorphous Zr–Ti–Cu–Ni–Be alloy. *Mater Sci Eng A* 334:33–40.
- Subhash G, Zhang H, Li H (2003) Thermodynamic and mechanical behavior of Hafnium–Zirconium-based bulk metallic glasses. *Proceedings of the International Conference on Mechanical Behavior of Materials (ICM-9)*, Geneva, Switzerland, May 25–29, 2003
- Tracy CA (1987) A compression test for high strength ceramics. *J Test Eval* 15:14–19.
- Blumenthal WR, Gray GT III (1989) Characterizations of shock-loaded aluminum-infiltrated boron carbide cermets. *Proceedings of the American Physical Society Topical Conference*, Albuquerque, NM, August 14–17, 1989
- Blumenthal WR, Gray GT III (1989) Structure-property characterization of a shock-loaded boron carbide-aluminum cermet. *International conference on mechanical properties of materials at high rates of strain*, Oxford, UK, March 20, 1989
- Couque H, Albertini C, Lankford J (1993) Failure mechanisms in a unidirectional fibre-reinforced thermoplastic composite under uniaxial, in-plane biaxial and hydrostatically confined compression. *J Mater Sci Lett* 12:1953–1957.
- Coscolluela A, Cagnoux J, Collombet F (1991) Uniaxial compression of alumina: structure, microstructure, and strain rate. *J Phys IV* 1:C3–109–C103-116.
- Lankford J (1977) Compressive strength and microplasticity in polycrystalline alumina. *J Mater Sci* 12:791–796.
- Bruck HA, Christman T, Rosakis AJ, Johnson WL (1994) Quasi-static constitutive behavior of $Zr_{41.25}Ti_{13.75}Ni_{10}Cu_{12.5}Be_{22.5}$ bulk amorphous alloys. *Scr Metall Mater* 30:429–434.
- Lewandowski JJ (2001) Effects of annealing and changes in stress state on fracture toughness of bulk metallic glass. *Mater Trans* 42:633–637.
- Lewandowski JJ, Lowhaphandu P (2002) Effects of hydrostatic pressure on the flow and fracture of a bulk amorphous metal. *Philos Mag A* 82:3427–3441.
- Lowhaphandu P, Lewandowski JJ (1998) Fracture toughness and notched toughness of bulk amorphous alloy: Zr–Ti–Ni–Cu–Be. *Scr Mater* 38:1811–1817.
- Lowhaphandu P, Ludrosky LA, Montgomery SL, Lewandowski JJ (2000) Deformation and fracture toughness of a bulk amorphous Zr–Ti–Ni–Cu–Be alloy. *Intermetallics* 8:487–492.
- Lowhaphandu P, Montgomery SL, Lewandowski JJ (1999) Effects of superimposed hydrostatic pressure on flow and fracture of a Zr–Ti–Ni–Cu–Be bulk amorphous alloy. *Scr Mater* 41:19–24.
- Yuan F, Prakash V, Lewandowski JJ (2007) Spall strength and Hugoniot elastic limit of a Zirconium-based bulk metallic glass under planar shock compression. *J Mater Res* 22:402–411.
- Shazly M, Prakash V, Lerch B (2006) High strain-rate compression of ice. *National Aeronautics and Space Administration*, Cleveland, OH.